On the physics of the Agulhas Current:
steady retroflection regimes

Henk A. Dijkstra and Wilhelmus P.M. de Ruijter

Institute for Marine and Atmospheric research Utrecht

Utrecht University

Utrecht, the Netherlands

Revised for J. Phys. Oceanography

Version of February 19, 2001

Corresponding Author:

Henk A. Dijkstra

Institute for Marine and Atmospheric research Utrecht

Department of Physics and Astronomy

Utrecht University

Princetonplein 5, 3584 CC Utrecht

The Netherlands

Phone: -31-30-2533858; Fax: -31-30-2543163

Email: dijkstra@phys.uu.nl

Abstract

From previous model studies, it has become clear that several physical mechanisms may be at work in the retroflection of the Agulhas current. Here, a systematic study of steady barotropic flows connecting the Indian Ocean and South Atlantic Ocean in several idealized set-ups is performed. By solving directly for the steady circulation with continuation methods, the connection between different retroflection regimes can be monitored as external conditions, such as the wind forcing, bottom topography as well as parameters, for example the lateral friction and layer depth, are changed. To distinguish the different steady retroflecting flows, an objective measure of the degree of retroflection, a retroflection index $\mathcal{R}$, is introduced. By monitoring $\mathcal{R}$ along a branch of steady solutions, using the horizontal friction as control parameter, several steady retroflecting regimes are found. At large friction there exist stable steady states with viscously dominated retroflection. When friction is decreased, inertial effects become more dominant and eventually unstable steady states with strong retroflection characteristics exist. Within this framework, different results from earlier studies can be reconciled.

1   Introduction

The Agulhas Current which rushes poleward in the Southwest Indian Ocean, suddenly changes its course near 20 $°E$, and retroflects back eastward (Gordon et al., 1987; Jacobs and Georgi, 1977; Lutjeharms and van Ballegooyen, 1988). Because of this retroflection, the volume exchange between the Indian Ocean and the Atlantic Ocean due to the Agulhas Current is relatively small, i.e. about 10% of the Agulhas transport. Within the Agulhas retroflection region, the flow has a strong variability and about six times every year a large ring is separated from the main current that propagates westward into the South Atlantic (Feron et al., 1992; Gordon and Haxby, 1990). An overview of the current state of knowledge with estimates of exchanges of mass, heat and salt has been given in a recent review (De Ruijter et al., 1999). Although the exchange due to the rings is small, it may be sufficiently large to cause changes in the Atlantic thermohaline circulation since the properties of the Indian Ocean water are substantially different from those in the Atlantic (Gordon, 1985; Weijer et al., 1999). Paleoceanographic studies have indicated that this exchange has varied significantly in the past (Howard and Prell, 1992), although a 'supergyre' fully connecting the Indian and Atlantic probably never existed.

The physics responsible for the retroflection and ring formation is still under debate. The Agulhas Current is the western boundary current of the Indian Ocean and as such has been studied with classical linear Sverdrup-Munk theory (De Ruijter, 1982), using an idealized model of the Indian-Atlantic domain. The geographic distribution of the wind stress curl is central to the global circulation pattern over the Indian-Atlantic Ocean. The observed annual mean of the wind stress curl remains positive as far south as 45 $°S$, whereas the continental shelf of Africa ends at $\theta_c = 37$ $°S$. Hence, beyond the latter latitude the Agulhas Current finds itself in a free ocean and, in a pure

frictional model, it moves around the tip of Africa and connects to the South American coast in a frictional shear layer (De Ruijter, 1982). Hence, for realistic values of the lateral friction, pure frictional barotropic processes cannot explain the retroflection of the Agulhas Current.

A weakly nonlinear extension of the Sverdrup-Munk theory (De Ruijter, 1982) indicates that the Agulhas Current may overshoot the latitude θ_c by a few hundred kilometer. This inertial overshoot is able to choke the gap between θ_c and the latitude of zero wind stress curl. In addition, the planetary vorticity gradient adds positive relative vorticity to fluid elements moving southwards, which is compensated by negative relative vorticity. The latter eventually leads to an eastward turning flow which provides a plausible mechanism of retroflection. This effect of the inertial overshoot and subsequent retroflection was confirmed in barotropic (De Ruijter and Boudra, 1985) and baroclinic (Boudra and De Ruijter, 1986) numerical models using an idealized geometry. By decreasing the layer depth in the barotropic case, the effect of inertia is increased and both gyres in the South Atlantic and Indian Ocean become more and more disconnected. Although new features, such as a center of recirculation in the retroflection region, were found in the two-layer model (Boudra and De Ruijter, 1986) the same physics is involved in the retroflection.

Continuing on the work of De Ruijter and Boudra (1985) and Boudra and De Ruijter (1986), an extensive parameter study was performed on the same configuration in Boudra and Chassignet (1988) and Chassignet and Boudra (1988). In the barotropic version of the model, a steady state is found at large horizontal friction ($A_H = 3300$ m^{2}s^{-1}). This state shows retroflection characteristics because the viscous boundary layer is quite thick. The other simulations were performed with small horizontal friction ($A_H = 330$ m^{2}s^{-1}), resulting in a strong variable flow of which the time mean shows

4

inertially controlled retroflection, similar to that in De Ruijter and Boudra (1985). Most of the other simulations focus on the role of baroclinic effects on the retroflection and dynamics of ring formation.

In the numerical studies above, the horizontal dimension of the basin is about 2000 km, which is relatively small with respect to reality. Matano (1996) considered the same problem within the domain $[-55 \, ^\circ S, -15 \, ^\circ S] \times [0 \, ^\circ E, 120 \, ^\circ E]$, using realistic bathymetry and geometry within barotropic and baroclinic versions of the Princeton Ocean Model (POM). No realistic retroflection is found in a flat bottom basin, but substantial retroflection is obtained when bottom topography is included. Inertia does not seem to be able to move the flow significantly southwards. However, topography is shown to be able to stear the flow and to guide the current eastward, which provides an alternative mechanism of retroflection (Lutjeharms and van Ballegooyen, 1984; Matano, 1996). The difference between the results in Matano (1996) and De Ruijter and Boudra (1985) cannot be deduced by comparing the Rossby number based on the basin length scale. In this case, $Ro = \tau_0/(\rho H \beta_0^2 L^3)$, where τ_0 is a typical amplitude of the wind stress, ρ the density, β_0 the strength of the planetary vorticity gradient, L the horizontal length scale and H the layer thickness. Although Ro is indeed much smalller in Matano (1996) – where the domain scale of the flow is the radius of the earth – than in De Ruijter and Boudra (1985), the characteristic horizontal length scale of the flow is much smaller in key regions and hence Ro is not a good measure for the magnitude of inertia in the flow.

In eddy-resolving general circulation models (Stammer et al., 1994; Lutjeharms and Webb, 1995) the retroflection of the mean Agulhas Current is reasonably simulated. For example, in the POCM model (Stammer et al., 1994), the Agulhas has a realistic transport of 66 Sv and it indeed retroflects near $20°E$ (De Ruijter et al., 1999). In

these models, several other factors contribute to the retroflection, in particular vortex stretching due to the deformation of isopycnals (Boudra and Chassignet, 1988). However, no detailed analyses of the dominant balances from the results of these models is known to resolve which mechanism is dominant.

These results above indicate that the physics of the retroflection of a current along a coastline as South-Africa is quite a complex problem. The sensitivity to the wind stress, shape of topography and parameters all question whether a broad parameter regime of (quasi-)steady separation can be found as observed in reality. More fundamental studies (Nof and Pichevin, 1996) have pointed to constraints which should be satisfied if a steady separation is dynamically realized within a barotropic context and suggest that this is not possible (Pichevin et al., 1999). Under a rather restricted set of constraints, for example the condition that the return flow does not meander, time-dependent phenomena, such as ring formation, are essential to the existence of retroflection.

Using new tools of analysis, we here consider the steady barotropic problem within a shallow water model. Continuation methods are used to follow branches of steady states through parameter space (and for several geometrical configurations) such that changes due to different physical processes can be monitored along a continuous path. This approach has proven valuable to study separation dynamics of other western boundary currents, such as the Gulf Stream (Schmeits and Dijkstra, 2000). The central problem addressed in this study is the reason for the different views of retroflection arising from the De Ruijter and Boudra (1985) and Matano (1996) results.

To have a more objective measure of retroflection, we define a retroflection function $R(\phi)$ and from this derive a retroflection index $\mathcal{R}$. Such an index does not seem to have been defined in the literature. From actual observations, one may not be very

motivated to do so; the mean Agulhas retroflection seems to have hardly varied over the last decades. Apart from the fact that it may have varied over longer time scales, such an objective measure is essential to quantify the effects of key physical processes on the retroflection characteristics. Basically, the retroflection index will be followed in parameter space as parameters, forcing and external conditions, such as the geometry, are varied. Both configurations in De Ruijter and Boudra (1985) and Matano (1996) will be studied with focus on the different dependence of the retroflection index on the lateral friction parameter. The results of both configurations can be reconciled by realizing that both are in different retroflection regimes. In addition, the results show that inertially retroflecting steady currents do exist, although these are unstable. This will be shortly discussed in view of the hypothesis of Nof and Pichevin (1996).

2   The barotropic shallow water model

2.1   Formulation

Consider an ocean basin with a horizontal domain $\mathcal{V}$ and bounded by a closed contour Γ. The density of the ocean is constant and the flow is driven by a wind stress $\tau_*(\phi,\theta) = \tau_0(\tau^\phi,\tau^\theta)$, where τ_0 is its amplitude and (τ^ϕ,τ^θ) provides the spatial pattern. The subscript * indicates dimensional quantities. Bottom topography is prescribed by a function $z_* = h_{b*}(\phi,\theta)$ and the free surface is indicated by $z_* = \eta_*(\phi,\theta,t)$. In the usual notation, the velocities in eastward and northward directions are indicated by u_* and v_*, respectively and $h_* = \eta_* - h_{b*}$ is the thickness of the water column (with equilibrium value H). Lateral friction, with lateral friction coefficient A_H is the only dissipative mechanism in the model. With r_0 denoting the radius of the earth, the governing shallow water equations are non-dimensionalized using scales r_0, H, U, r_0/U

7

and τ_0 for length, layer depth, velocity, time and wind stress, respectively, where r_0 is the radius of the earth and become

$$-v\sin\theta = \begin{aligned}\epsilon\left(\frac{\partial u}{\partial t} + \frac{u}{\cos\theta}\frac{\partial u}{\partial\phi} + v\frac{\partial u}{\partial\theta} - uv\tan\theta\right)\\ -\frac{\epsilon F}{\cos\theta}\frac{\partial\eta}{\partial\phi} + E\left(\nabla^2 u - \frac{u}{\cos^2\theta} - \frac{2\sin\theta}{\cos^2\theta}\frac{\partial v}{\partial\phi}\right) + \alpha\frac{\tau^\phi}{h}\end{aligned} \quad (1a)$$

$$+u\sin\theta = \begin{aligned}\epsilon\left(\frac{\partial v}{\partial t} + \frac{u}{\cos\theta}\frac{\partial v}{\partial\phi} + v\frac{\partial v}{\partial\theta} + u^2\tan\theta\right)\\ -\epsilon F\frac{\partial\eta}{\partial\theta} + E\left(\nabla^2 v - \frac{v}{\cos^2\theta} + \frac{2\sin\theta}{\cos^2\theta}\frac{\partial u}{\partial\phi}\right) + \alpha\frac{\tau^\theta}{h}\end{aligned} \quad (1b)$$

$$\frac{\partial h}{\partial t} + \frac{1}{\cos\theta}\left(\frac{\partial(hu)}{\partial\phi} + \frac{\partial(hv\cos\theta)}{\partial\theta}\right) = 0 \quad (1c)$$

On the boundary Γ of the domain no-slip conditions are prescribed, i.e.

$$(\phi,\theta)\;\varepsilon\;\Gamma:\quad u = v = 0 \quad (2)$$

The parameters in these equations are the Rossby number ϵ, the inverse Froude number F, the Ekman number E, and the wind stress coefficient α. Expressions for these parameters are

$$\epsilon = \frac{U}{2\Omega r_0}\;;\; F = \frac{gH}{U^2}\;;\; E = \frac{A_H}{2\Omega r_0^2}\;;\; \alpha = \frac{\tau_0}{2\Omega\rho HU} \quad (3)$$

where Ω is the angular velocity of the earth.

2.2 The retroflection index $\mathcal{R}$

A retroflection function, $R(\phi;\theta_0)$, based on the southward volume transport (Φ_s) of the Agulhas current at a latitude θ_0 and the westward volume transport (Φ_w) over a section south of the South African continent at a longitude ϕ is defined (Fig. 1). If retroflection is weak, one would expect that the ratio of both transports is nearly unity, whereas

8

if Φ_w is substantially smaller than Φ_s, the flow has retroflection characteristics. More precisely, we consider the function $R(\phi; \theta_0)$ for fixed latitude θ_0 defined by

$$R(\phi; \theta_0) = 1 - \frac{\Phi_w(\phi)}{\Phi_s(\theta_0)} \tag{4a}$$

$$\Phi_s(\theta_0) = max_\phi \int_{\phi_W}^{\phi} (-h \ v \ \cos \ \theta) \ d\phi \tag{4b}$$

$$\Phi_w(\phi) = max_\theta \int_{\theta_N}^{\theta} (-hu) \ d\theta \tag{4c}$$

where the integrals are taken over specified sections defined by the domain $\theta_S, \theta_N, \phi_W$ and ϕ_E, with ϕ_W being a longitude on the eastcoast of the African continent for given θ_0.

If ϕ_c is the longitude of the southern tip of the continent the different flows can be classified according to the behavior of the retroflection function near ϕ_c. If $\mathcal{R} = R(\phi_c; \theta_0) \approx 0$, the flow will have a complete leakage, while if $\mathcal{R} \approx 1$, then a complete retroflection has occured. For intermediate cases, partial retroflection occurs and the degree depends on the value of $\mathcal{R}$ (Fig. 1). Note that $\mathcal{R}$ can be negative if recirculations in the flow occur. Apart from this, $\mathcal{R}$ appears to be a reasonable measure to monitor the degree of retroflection close to the tip of the continent and we will call this the retroflection index.

2.3 Numerical methods

For the shallow water model, a finite difference central discretization was used on a staggered Arakawa-C grid. To ensure overall mass conservation, an integral condition for h over the domain $\mathcal{V}$ is implemented (Schmeits and Dijkstra, 2000), i.e.

$$\int_{\mathcal{V}} h \ \cos \theta \ d\phi d\theta = | \ \mathcal{V} \ | \tag{5}$$

9

where $|\mathcal{V}|$ is the (dimensionless) area of the domain (note that the layer depth is scaled with H).

Discretization of the steady state solutions leads to a set of nonlinear algebraic equations of the form

$$\mathbf{F}(\mathbf{u}, \mathbf{p}) = 0 \tag{6}$$

Here $\mathbf{u}$ is a d-dimensional vector consisting of the unknowns at the gridpoints, $\mathbf{p}$ is the p-dimensional vector of parameters and $\mathbf{F}$ is a nonlinear mapping from $R^d \times R^p \to R^d$, where d indicates the number of degrees of freedom. To determine branches of steady solutions of the equations (6) as one of the parameters (say μ) is varied, the pseudo-arclength method is used (Keller, 1977). The branches $(\mathbf{u}(s), \mu(s))$ are parametrized by an 'arclength' parameter s. An additional equation is obtained by 'normalizing' the tangent

$$\dot{\mathbf{u}}_0^T(\mathbf{u} - \mathbf{u}_0) + \dot{\mu}_0(\mu - \mu_0) - \Delta s = 0 \tag{7}$$

where $(\mathbf{u}_0, \mu_0)$ is an analytically known starting solution or a previously computed point on a particular branch and Δs is the steplength. Note that with these techniques we are able to find not only the stable steady solutions, but also unstable ones since the Newton-Raphson technique finds isolated solutions regardless of their stability (Dijkstra et al., 1995).

To determine the linear stability of a steady state $\bar{\mathbf{u}}$, perturbations $\hat{\mathbf{u}}e^{\sigma t}$ are considered and linearizing the equations around $\bar{\mathbf{u}}$ gives a discretized eigenvalue problem of the form

$$\mathcal{A}\hat{\mathbf{u}} = \sigma \mathcal{B}\hat{\mathbf{u}} \tag{8}$$

where $\mathcal{A}$ is a nonsingular, non-symmetric $d \times d$ matrix. Through Dirichlet boundary conditions and/or the incompressibility condition, $\mathcal{B}$ may become singular. The eigenvalue problem is solved with the Jacobi-Davidson QZ-method (Sleijpen and Van der

Vorst, 1996). With this method, a few eigensolutions can be computed near a specific target.

3 Retroflection in an idealized basin

Our starting point is a similar situation to that studied in De Ruijter and Boudra (1985). Aim is to investigate whether steady retroflecting currents can be obtained in this configuration.

3.1 Model set-up

The domain chosen is $\phi_W = 10$, $\phi_E = 32$, $\theta_S = -42$ and $\theta_N = -30$, and the basin has a flat bottom. Although the zonal size of the domain varies with latitude (from about 2100 km at the northern boundary to about 1800 km at the southern boundary) it has about the same dimensions as in De Ruijter and Boudra (1985), with a meridional extent of 1300 km. A rectangular continent is present over the domain $\phi_W = 19.5$, $\phi_E = 20.5$, $\theta_S = -35$ and $\theta_N = -30$.

The wind stress forcing is prescribed as an analytical profile of the form

$$\tau^\phi(\theta) = \cos \ \pi(6.37(\theta - \theta_*)) \ ; \ \tau^\theta = 0 \tag{9}$$

which is shown in Fig. 2 for $\theta_* = -39.5$. The amplitude was chosen similar to that in De Ruijter and Boudra (1985), i.e. $\tau_0 = 0.2 \ Pa$. In this way, the maximum westerly wind stress is located at $\theta = -39.5$, i.e. about 400 km south of the tip of the continent. Although the wind stress curl is not exactly zero at this location (because of the spherical coordinates), the deviation is small because of the small basin size.

Standard values of both dimensional and non-dimensional parameters are given in Table 1. To compare these values with those in De Ruijter and Boudra (1985), we note

that their characteristic velocity scale is $U = \tau_0/(\rho_0 H \beta_0 L)$, with $L = 1000 \; km$ and $\beta_0 = 1.9 \times 10^{-11}$. Hence, the Rossby number Ro for a depth $H = 1000 \; m$ is about 5.5×10^{-4}. With the choice $A_H = 330 \; m^2/s$ as in De Ruijter and Boudra (1985), the reference value of the Ekman number is $E = 5.0 \times 10^{-8}$. In the results below, the Ekman number will be used as a control parameter and be varied over several orders of magnitude. All results below are presented as bifurcation diagrams where the retroflection index $\mathcal{R}$, computed as

$$\mathcal{R} = 1 - \frac{\Phi_w(20)}{\Phi_s(-35)} \tag{10}$$

is monitored versus E.

3.2   Results: effects of horizontal resolution

For standard values of parameters, bifurcation diagrams are plotted for four different resolutions $(1/4°, 1/5°, 1/6°$ and $1/7°)$ in Fig. 3. Starting at the high friction end (large E), the retroflection index decreases with decreasing E and for different resolutions a comparable retroflection index is obtained down to about $E = 2 \times 10^{-7}$. However, for smaller values of E the curves start to diverge significantly, but all of them show an increasing $\mathcal{R}$ with decreasing E. Although the solutions seem to have been converged at about $1/6°$, they can only be computed for values of E down to about 8.0×10^{-8}, which is still above the standard value (5.0×10^{-8}) used in De Ruijter and Boudra (1985). For smaller values of E, the Newton-Raphson process, which is used to compute the steady states, gives trouble to converge, likely because of resolution problems.

For different horizontal resolutions and comparable Ekman number, similarly looking flows are obtained, with all flows having a frictional shear layer extending to the western boundary of the domain, with a return flow which is extensively meandering. Details differ near the continental boundary, in particular the Atlantic side, and a

12

slightly different angle between the Agulhas Current and the continent. A solution for the anomalies in layer thickness $\tilde{h}$ is plotted in Fig. 4 for $1/6°$ resolution. The position of the saddle point just below the continent shifts slightly westward as the resolution is changed. Since the retroflection index is computed at a location close to the southern tip of the continent, small changes in the resolution will give rather large changes in retroflection index.

3.3   Results: inertial retroflection

The results above indicate that for solutions computed on $1/4°$ (as is the resolution for most results in De Ruijter and Boudra (1985) and Boudra and Chassignet (1988)) the Ekman number should be larger than $E = 2 \times 10^{-7}$. Note that the Ekman number actually used in these early studies is 5×10^{-8}. Fortunately, this still allows us to explore the effect of changes in layer thickness H, just as in De Ruijter and Boudra (1985), to study the effect of inertia on the steady flows. Note that H influences both the input of vorticity by the wind stress (through the parameter α) as well as the external Rossby deformation radius (through the parameter F). Bifurcation curves are shown in Fig. 5, with patterns of the layer thickness anomaly $\tilde{h}$ in Fig. 6.

At large horizontal friction, E relatively large, all curves start out with a relatively large retroflection index. With decreasing E, the retroflection decreases, indicating more Agulhas leakage. For each of the layer thicknesses, there exists a value of E where the retroflection index is minimal. For smaller H, this minimum shifts to larger values of E. For $H = 2000 \; m$, this minimum occurs at about 1.0×10^{-7}, but is not shown (because we restrict to $E > 2 \times 10^{-7}$). Solutions for the layer thickness anomaly near $E = 2 \times 10^{-7}$ indicate that the mean Agulhas Current rotates in a counterclockwise direction with respect to the continent as H is decreased (Fig. 6a-c). For the smallest

layer thickness, it overshoots and near turns back onto itself in a large meander. The latter solution has similar features as the solutions in the frictionless model of Ou and De Ruijter (1986).

The linear stability boundary of the steady states for $H = 1000$ m and $H = 250$ m is also indicated in Fig. 5 as a marker on the branch (the triangle). For values of E larger than this stability boundary, the steady states are stable. This is in agreement with the result in Boudra and Chassignet (1988) for $E = 5.0 \times 10^{-7}$ and $H = 1000$ m (labelled NLIN2 in their Table 1). Indeed, for this value E, a stable steady state must be obtained according to Fig. 5 since it is unique and the system is dissipative. For $H = 1000$ m, the steady state undergoes a Hopf bifurcation at $E = 2.5 \times 10^{-7}$ (Guckenheimer and Holmes, 1983; Dijkstra, 2000). If a transient flow is computed at $E = 2.0 \times 10^{-7}$, which is in the unstable regime, a periodic solution is obtained. If one computes the time mean state of this periodic orbit, it very much looks like the unstable steady state calculated at $E = 2.0 \times 10^{-7}$. Hence, the steady state pattern, although it is unstable, is still very relevant because the trajectory (the transient flow) remains in its neighborhood.

When the Ekman number is further decreased, more of these instabilities occur and the complexity of the time-dependent flow increases. Note that we actually do not compute steady states for values of E smaller than $E = 2.0 \times 10^{-7}$, because we think that the resolution is not adequate in this regime. For very much smaller E, for example the result NLIN1 in Boudra and Chassignet (1988) which is at $E = 5 \times 10^{-8}$, the relation between the steady states and the transient flow computations becomes *a priori* more unclear, and strongly depends on the degree of instability of the underlying steady state. We do not address this question in the present paper and seek no correspondence with steady states and time mean flows in this small Ekman number regime ($E \ll 2.0 \times 10^{-7}$).

14

The mechanism of the instability of the steady flows, the transition to (complex) time-dependent behavior and its relation to ring formation will be reported elsewhere.

These results support the view that there are two steady retroflection regimes, one frictional (with a thick frictional western boundary layer) regime and an inertial regime (with a strong inertial overshoot). Both regimes are separated by a transition regime, where the frictional shear layer is thinning, while the inertial overshoot is too small to let the current separate from the continent: consequently, the retroflection is weak.

To confirm this view, the vorticity balances along the sections of the flow from which the retroflection index is computed are investigated. By taking the discrete curl of the discretized momentum equations of the shallow water model, the terms in the vorticity equation satisfy a closed balance up to six digits. In the figures below, these terms are labelled I (inertia), B (β-effect), F (friction) and W (wind) such that the balance is written as

$$\frac{\partial \zeta}{\partial t} = -(I + B - F - W) = 0 \qquad (11)$$

where ζ is the relative vorticity. From the signs of each quantity, it can now be determined whether a physical process adds positive or negative local relative vorticity to the flow. For the four solutions in Fig. 6 these terms are plotted in Fig. 7 (at $\theta = -35$) and Fig. 8 (at $\phi = 20$). We have chosen to plot the terms as they appear in (11), i.e. $-F$ and $-W$ are plotted, such that every negative (positive) quantity in the figure gives a positive (negative) tendency of the relative vorticity in the flow. When all terms are added as plotted, net zero vorticity input results.

In the zonal section, the vorticity input by the wind stress is constant and positive for all cases. This is a consequence of the constant wind stress curl and the fact that the maximum westerly wind occurs at a more southerly location. On the eastern part of the basin, the flow is northward and through the β-effect a fluid element aquires

15

negative vorticity. In this region, a Sverdrup balance is found since the effect of friction and inertia are small. Near the western boundary, the β-term changes sign, because the flow is southward. There is a small interval where friction is still small and the β-effect balances inertia, but friction is a major term in the boundary layer balance which is of typical nonlinear Munk-type. With decreasing layer depth, the frictional Munk bondary layer thickness becomes smaller. The interval over which pure inertial balances exist (with a minor role for friction) becomes larger (Fig. 7c). For the smallest layer thickness, even the Sverdrup interior in the eastward part of the basin gets strongly modified through the recirculation areas (Fig. 7d).

In the meridional section, the vorticity input by the wind changes from negative to positive when going northward, the curl being zero at about $\theta = -39.5$ (Fig. 8a). Inertia appears important for all cases near the continental boundary, but its effect on the vorticity balance changes as the Agulhas current gets stronger with decreasing layer depth (Fig. 8b-c). Although friction is of considerable magnitude in Fig. 8d, the negative vorticity input due to inertia is too strong to be balanced by friction. Hence the β-effect is needed, with a net result of positive vorticity, to close the balance and southward motion results. The earlier separation and the turning of the current are seen (Fig. 8b-c) as the shift in the maximum of I to higher latitudes. The retroflection characteristics at small E and small H can be deduced as being caused by inertial overshoot and the balances are consistent with the original mechanism proposed by De Ruijter and Boudra (1985).

4 Retroflection in a realistic basin

Having established that the effect of inertia is visible in the steady state barotropic solutions in the De Ruijter and Boudra (1985) set-up and indeed contributes to enhanced

retroflection, as measured by $\mathcal{R}$, we now consider the more realistic case studied by Matano (1996).

4.1   Model set-up

As standard domain, we choose the a flat-bottomed region $0°\ E - 80°\ E$ and $60°\ S - 20°\ S$, which is quite similar to that considered by Matano (1996). Standard resolution is $1/2°$ both in zonal and meridional direction and the grid (160×80 points) is equidistant. The annual mean wind stress field from Trenberth et al. (1989) is interpolated on this grid and used to force the model. A plot of both zonal and meridional components of this wind field is shown in Fig. 9. Maximum westerly wind stress occurs at about $\theta = -45$ and for $\phi = 20$, the wind stress curl becomes zero near $\theta = -47.5$. The meridional component of the wind is southward over most of the domain, with maxima near $\theta = -45$. Standard values of parameters used in the model are given in Table 2, with $E = 3.0 \times 10^{-7}$ as reference value for the Ekman number (Matano, 1996).

4.2   Frictional versus inertial regime

The retroflection index $\mathcal{R}$ is computed from sections at $\theta_0 = -35$ and $\phi = 20$. Four different layer depths are considered, i.e. $500, 1000, 2000\ m$ and an average depth computed from a smoothed bathymetry ($H_{av} \approx 4000\ m$). The retroflection index $\mathcal{R}$ is plotted for these cases in Fig. 10 and although highest values are again obtained at large values of E, all calculated retroflection indices are very small. A typical solution in this viscous regime is plotted for $E = 1.0 \times\ 10^{-5}$ and $H = 1000\ m$ in Fig. 11a. Some retroflection is seen of the western boundary current present in a thick frictional boundary layer. With decreasing friction, $\mathcal{R}$ decreases (Fig. 10) and similar to the small basin case above, it goes through a minimum at a certain value of E. For even smaller

17

E, $\mathcal{R}$ increases slightly with decreasing E, but it is still very small at the reference value $E = 3 \times 10^{-7}$. No stability boundaries were determined for these flows.

Near this reference value, all solutions have no retroflection at all near the tip of South Africa (Fig. 11b-d). Note that the solutions have a fairly good correspondence to those shown in Matano (1996). The retroflection index is negative in this regime, i.e. maximum transport westward over $\phi = 20$ becomes larger than that southward over $\theta = -35$ because of the local wind-driven transport generated over the retroflection region (Fig. 11c-d). The three solutions (Fig. 11b-d) differ most near the western boundary of the computational domain, with larger recirculation for the smaller layer case (Fig. 11b).

Plots of terms in the vorticity balances along the same zonal and meridional sections from which the retroflection index is computed are presented in Fig. 12. Along the zonal section for the large E case (Fig. 12a), there is a nearly linear Munk layer near the African east coast with a Sverdrup balance over the rest of the domain. Similar balances hold over the meridional section (Fig. 12c) for this case; one can see that the wind input has comparable magnitude in this case with a sign change near $\theta = -47$.

For a smaller Ekman number a nonlinear Munk layer develops (Fig. 12b) in the zonal section near the continental boundary, with similar balances as for the small basin case (e.g. compare Fig. 7c). However, in the meridional section, only a weakly nonlinear Munk layer is present in small Ekman number case (Fig. 12d). There is an essential difference between the balances in the latter case and those in, for example, Fig. 8c. In the small basin case, there is no interval of large input of negative vorticity due to inertia. In other words, the inertial overshoot is still very weak and there is no need for southward motion to get compensating positive vorticity from the β-effect. Hence, based on the latter vorticity balance, one can conclude that an inertially controlled

18

regime has not been reached at the value of $E = 3.0 \times 10^{-7}$ and $H = 1000$ m, which is the standard case in Matano (1996).

5 Discussion

Within a barotropic shallow water model, the steady retroflection of the Agulhas Current has been studied. Central motivation was to resolve the apparently different points of view concerning the dominant mechanism of retroflection in earlier studies (De Ruijter and Boudra, 1985; Matano, 1996). Thereto an objective measure of retroflection is defined, the retroflection index $\mathcal{R}$. A major advantage in the approach using continuation methods is that steady solutions can be monitored over a large range in parameter space and that solutions can be found regardless of their stability.

The Ekman number E, related to the horizontal friction coefficient, was chosen as control parameter. In the configuration used in De Ruijter and Boudra (1985), retroflecting steady currents are found in two regimes, either for very large E or below a certain value of E. In the intermediate regime, $\mathcal{R}$ decreases with E and no realistic steady retroflection can be obtained. As already pointed out by De Ruijter and Boudra (1985), an important ingredient to actual retroflection is a mechanism to get the mean Agulhas Current enough southward into the open ocean. With large friction, the western boundary layer is so thick that this distance is bridged by viscous (subgrid scale) processes. Through this 'frictional choking', the flow comes into the range where it can be connected to the far field flow generated by the winds over the South Indian ocean. In the inertial regime, the inertial overshoot bridges this gap with similar consequences for retroflection. In the intermediate regime, the viscous shear layer is thinning which limits the frictional choking while simultaneously the inertial overshoot is still to small: no retroflection is obtained. This explains the existence of the minimum in the

retroflection index with E, say E_c. The value of E_c indeed increases with decreasing layer thickness since the inertial contributions become larger (larger Rossby number). This view is also confirmed from the local vorticity balances along the sections from which the retroflection index was computed. Strong inertial overshoot is characterized by an inertially dominated balance, with the β-term (B) balancing the inertia term (I) and a minor role for friction.

One could think that these two regimes of retroflection were already found in Boudra and Chassignet (1988), based on the simulations NLIN1 and NLIN2. Although one may have doubt that, without hindsight to the present results, one would be able to identify regimes based on only two points in the parameter space, there is a more subtle point in that here the regimes are steady. From the solution NLIN1 (at $E = 5.0 \times 10^{-8}$) one does not know whether (i) already the steady balances allow for retroflection characteristics and the trajectory circles around this unstable steady state due to interacting instabilities, or (ii) whether rectification processes due to the instabilities cause the retroflection characteristics, with the unstable steady state having none. In this paper, a clear answer is given: retroflection characteristics are already in the steady balances.

Clearly, the configuration of De Ruijter and Boudra (1985) is, for small layer depths, in the inertial regime, although a resolution of 40 km is likely too coarse to fully resolve the flows in this regime. The results here show that at least $1/6°$ is needed to accomplish this for layer depths larger than 1 km. The reason why Matano (1996) does not find substantial retroflection for his configuration is that the inertially controlled regime has not been reached yet. His value of E is seen to be in the transition regime, as can be seen from the value of E_c computed for the different cases and the local vorticity balances. Does indeed retroflection occur when this regime is eventually reached ? Within this model, the question turns out to be difficult to answer. The results for the

small basin case already indicate that high resolution is needed to resolve the flow in this regime. We performed one additional set of computations with higher resolution $1/4° \times 1/3°$ for a basin over the domain $[0, 80] \times [-55, -25]$, with a layer thickness of $H = 500\ m$, but found no inertially controlled retroflection for E down to 10^{-7}. However, our expectation is that if one repeats the calculations of Matano with much higher resolution and smaller Ekman number, the effects of inertia would be much more dominant. This view is consistent with results of separation of the Gulf Stream, where reasonable separation is found only below $0.1°$ horizontal resolution (Smith et al., 2000). This reconciles the different views on the dominant mechanism of retroflection in both barotropic model studies.

It is interesting that examples of strong retroflecting currents are found here in the De Ruijter and Boudra (1985) configuration, while the 'retroflection paradox' raised in Nof and Pichevin (1996) seems to suggest that these should not exist. The argument of Nof and Pichevin (1996) is regardless of any stability considerations. It is a claim about non-existence, so even when the flows here are unstable, they should not exist within their framework. This apparent contradiction needs more analyis to resolve, since it may indicate that one of the assumptions in their set-up is not satisfied, very likely being the requirement that the return flow does not meander. Otherwise, there may be some singular behavior in the limit of zero friction. Note that it will be difficult to resolve this issue from numerical model studies of time-dependent flows, since instabilities of the large scale flow immediately introduce temporal variability.

Although in the 'real' Agulhas current, effects of stratification and time-dependent phenomena are expected to be important (Boudra and Chassignet, 1988; Chassignet and Boudra, 1988) it is still worthwhile to look at the sensitivity of barotropic processes controlling the retroflection. First issue is the sensitivity of the inertial regime with

respect to the shape and angle of the continent. For example, it seems reasonable that the continental shelf south of Africa must be taken into account in the real geometry as considered above. Is the inertially controlled retroflection regime reached sooner through a different continental shape? To investigate this an idealized continental shape was defined by

$$\theta = \theta_p + (\frac{\phi - \phi_p}{\gamma})^2 \tag{12}$$

which is one choice of the family of parabolic shapes suggested and used in De Ruijter (1982). In this equation, γ controls the width and angle of the continent and θ_p its southern tip. We considered the parameters $\gamma = 2.58$, with ϕ and θ given in degrees. In this case $\phi_p = 20$ and the extent of the land on $\theta = -20$ is $10°$. The flow was forced with the realistic wind stress field as in section 4.

For $H = 1000\ m$ and $\theta_p = -38.5$ two solutions for the layer thickness anomaly are shown in Fig. 13, for $E = 10^{-5}$ and $E = 4.4 \times 10^{-7}$. In the viscous regime, the southward extension of the continent promotes retroflection as is clear from the frictional choking mechanism: the boundary layer now extends farther southwards. The presence of the continent down to $\theta_p = -38.5$ also induces a weak recirculation to the west of the continent, but with relatively small amplitude (Fig. 13a). The retroflection index monotonically decreases with decreasing E down to the standard value ($E = 3.0 \times 10^{-7}$) indicating that, for this particular continental shape, the inertial regime is not reached sooner with decreasing E. This is also seen for the solution at relatively small E in Fig. 13b, where no retroflection is present. Computations for two other choices of γ show that even with different angles and widths of the continent the behavior of retroflection index with Ekman is the same. This is not unexpected as we are not yet in the inertial regime, where the effect of continental shape may become much more important (Ou and De Ruijter, 1986).

22

As a second aspect, bottom topography was considered through an extensively smoothed version of the ETOPO5 data set. Using the average depth H_{av}, a homotopy parameter p_b is introduced and the bottom topography is defined as

$$h_b = (1 - p_b)H_{av} + p_b h_{bs} \qquad (13)$$

where h_{bs} is the (smoothed) bottom topography of the basin. For $p_b = 0$ the flat bottomed (average depth) case is recovered and for each value of p_b, the average depth is the same. It turns out that the retroflection index is quite sensitive to the value of p_b and the degree of smoothing applied. In the large friction case, the effect of topography is to decrease the retroflection index, whereas in the small friction regime, the retroflection index increases for p_b up to 0.05. Qualitatively, the effect of topography may be to steer the current southward thus facilitating the connection to the eastward flow in the Indian Ocean (Matano, 1996). For larger values of p_b the flows become very sensitive to E and it is difficult to resolve these flows. Hence, we conclude that the effect of topography cannot be adequately studied within the present model set-up.

Another factor, which may influence the different separation regimes is the presence of the western no-slip boundaries in the model which are absent in reality, because of the presence of the Antarctic Circumpolar Current (ACC). Does the Antarctic Circumpolar Current promote retroflection and if yes, how? By using the shallow water model, the flow in the Southern Hemisphere from $[0, 360] \times [-80, 0]$ is computed for standard values of parameters and $E = 1.7 \times 10^{-5}$ (Fig. 14) using a resolution of $2°$. The presence of a nearby viscous eastward moving flow can be felt northward as far as the tip of Southern Africa, where it influences the 'far field' pressure gradient. Combined with the thickness of the Agulhas boundary layer it enhances the frictional choking effect, and promotes retroflection resulting in a 'good looking' retroflection. Actually, in course resolution models (resolution about $3°$), similar 'good looking' retroflecting Agulhas Currents are

seen (see for example, Cai and Greatbatch (1995)) likely because of similar physics.

To summarize, although this systematic study has not solved the retroflection problem of the Agulhas Current, it has given some clear answers on details of this problem, i.e.

(i) Depending on the value of the horizontal friction, there appear two (and only) two regimes of retroflection in the barotropic steady problem. These are a viscous regime and an inertial regime which are separated by an intermediate regime, where retroflection is weak. Inertial retroflection can hence occur within the steady balances and there is no need for rectification due to time-dependent processes. The existence of these regimes reconciles results of earlier studies and also indicates that to get into the inertial retroflection regime, high resolution and low friction are necessary. To study inertially barotropically controlled retroflection in the realistic basin, high resolution (likely up to 1/6°) appears necessary.

(ii) Good looking retroflection may be obtained in the viscous regime, but for the wrong physical reasons. At high friction, the frictional chooking effect establishes a barrier for any transport to the Atlantic. Although the picture may please coarse resolution modellers, the associated transport quantities, of importance in climate variability and the stability of the current may be totally wrong.

It is hoped that these results will provides guidelines for further studies into this intriguing problem.

Acknowledgements

References

Boudra, D. B. and E. P. Chassignet, 1988: Dynamics of the Agulhas retroflection and ring formation in a numerical model. I. The vorticity balance. *J. Phys. Oceanography*, **18**, 280–303.

Boudra, D. B. and W. P. M. De Ruijter, 1986: The wind-driven circulation in the South Atlantic-Indian ocean: II. Experiments using a multi-layer numerical model. *Deep-Sea Research*, **33**, 447–482.

Cai, W. and R. Greatbatch, 1995: Compensation for the NADW outflow in a global ocean general circulation model. *J. Phys. Oceanography*, **25**, 226–241.

Chassignet, E. P. and D. Boudra, 1988: Dynamics of the Agulhas retroflection and ring formation in a numerical model: II. Energetics and Ring formation. *J. Phys. Oceanography*, **18**, 304–319.

De Ruijter, W., 1982: Asymptotic analysis of the Agulhas and Brazil current systems. *J. Phys. Oceanography*, **12**, 361–373.

De Ruijter, W. and D. B. Boudra, 1985: The wind-driven circulation in the South-Atlantic Indian Ocean. I. Numerical experiments in a one-layer model. *Deep-Sea Research*, **32**, 557–574.

De Ruijter, W. P. M., B. A., S. S. Drijfhout, J. R. E. Lutjeharms, R. P. Matano, T. Pichevin, P. J. van Leeuwen, and W. Weijer, 1999: Indian-Atlantic interocean exchange: dynamics, estimation and impact. *J. Geophysical Res.*, **104**, 20,885–20,910.

Dijkstra, H. A., 2000: *Nonlinear Physical Oceanography*. Kluwer Academic Publishers, Dordrecht, the Netherlands.

Dijkstra, H. A., M. J. Molemaker, A. van der Ploeg, and E. F. F. Botta, 1995: An efficient code to compute nonparallel flows and their linear stability. *Comp. Fluids*, **24**, 415–434.

Feron, R. C. V., W. P. M. De Ruijter, and D. Oskam, 1992: Ring-shedding in the Agulhas Current system. *J. Geophysical Res.*, **97**, 9467–9477.

Gordon, A. L., 1985: Indian - Atlantic transfer of thermocline water at the Agulhas Retroflection. *Science*, **227**, 1030–1033.

Gordon, A. L. and W. F. Haxby, 1990: Agulhas eddies invade invade the South Atlantic: evidence from GEOSAT altimeter and shipboard CTD survey. *J. Geophysical Res.*, **95**, 3117–3125.

Gordon, A. L., J. R. E. Lutjeharms, and M. L. Gründlingh, 1987: Stratification and circulation at the Agulhas retroflection. *Deep-Sea Research*, **34**, 565–599.

Guckenheimer, J. and P. Holmes, 1983: *Nonlinear oscillations, Dynamical systems and Bifurcations of Vector Fields*. Springer Verlag, Berlin-Heidelberg, Germany.

Howard, W. R. and W. L. Prell, 1992: Late quaternary surface circulation of the southern Indian Ocean and its relationship to orbital variation. *Paleoceanography*, **7**, 79–117.

Jacobs, S. S. and D. T. Georgi, 1977: Observations on the southwest Indian/Antarctic ocean. *Deep-Sea Research*, **24**, 43–84.

Keller, H. B., 1977: Numerical solution of bifurcation and nonlinear eigenvalue problems. In *Applications of Bifurcation Theory*, Rabinowitz, P. H., editor. Academic Press, New York, U.S.A.

Lutjeharms, J. R. E. and R. C. van Ballegooyen, 1984: Topographic control in the Agulhas Current system. *Deep-Sea Research*, **31**, 1321–1337.

Lutjeharms, J. R. E. and R. C. van Ballegooyen, 1988: The Agulhas Current retroflection. *J. Phys. Oceanography*, **18**, 1570–1583.

Lutjeharms, J. R. E. and D. J. Webb, 1995: Modelling the Agulhas current system with the Fne Resolution Antarctic Model (FRAM). *Deep-Sea Research*, **42**, 523–551.

Matano, R. P., 1996: A numerical study of the agulhas retroflection: the role of bottom topography. *J. Phys. Oceanography*, **26**, 2267–2301.

Nof, D. and T. Pichevin, 1996: The retroflection paradox. *J. Phys. Oceanography*, **26**, 2344–2358.

Ou, H. W. and W. P. M. De Ruijter, 1986: Separation of an inertial boundary current from an irregular coastline. *J. Phys. Oceanography*, **16**, 280–289.

Pichevin, T., D. Nof, and J. R. E. Lutjeharms, 1999: Why are there Agulhas rings. *J. Phys. Oceanography*, **29**, 693–707.

Schmeits, M. J. and H. A. Dijkstra, 2000: On the physics of the 9 months variability in the Gulf Stream region: combining data and dynamical systems analysis. *J. Phys. Oceanography*, **30**, 1967–1987.

Sleijpen, G. L. G. and H. A. Van der Vorst, 1996: A jacobi-davidson iteration method for linear eigenvalue problems. *SIAM J. Matrix Anal. Appl.*, **17**, 410–425.

Smith, R. D., M. E. Maltrud, F. O. Bryan, and M. W. Hecht, 2000: Numerical simulation of the North Atlantic Ocean at $\frac{1}{10}^{\circ}$. *J. Phys. Oceanography*, **30**, 1532–1561.

Stammer, D. R., R. Tokmakian, A. Semtner, and C. Wunsch, 1994: How well does a $\frac{1}{4}^\circ$ global circulation model simulate large scale oceanic observations? *J. Geophysical Res.*, **101**, 25,779–25,811.

Trenberth, K. E., J. G. Olson, and W. G. Large, 1989: A global ocean wind stress climatology based on ECMWF analyses. Technical report, National Center for Atmospheric Research, Boulder, CO, U.S.A.

Weijer, W., W. P. M. De Ruijter, H. A. Dijkstra, and P. J. Van Leeuwen, 1999: Impact of interbasin exchange on Atlantic overturning. *J. Phys. Oceanography*, **29**, 2266–2284.

Figure Captions
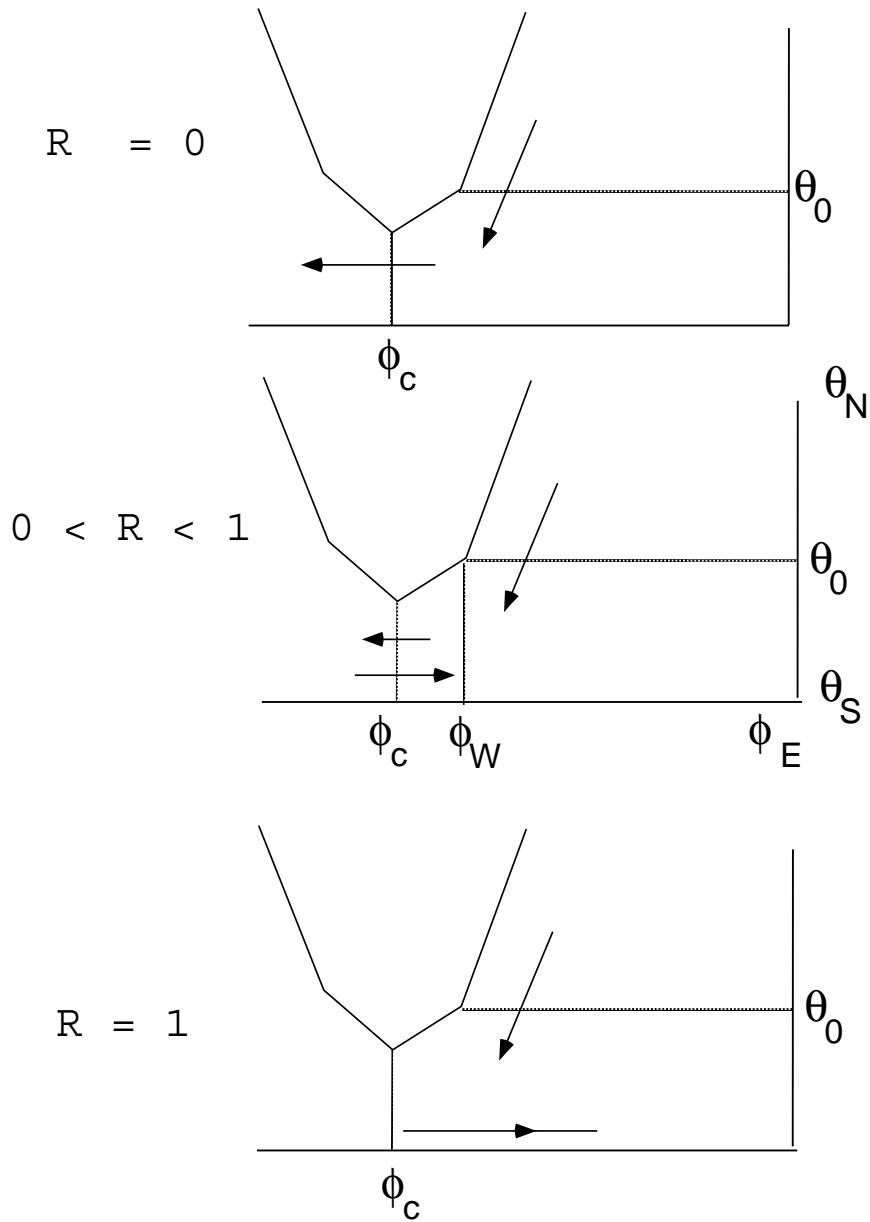
Fig. 1.

Sketch illustrating the meaning of the retroflection index, which is based on the different volume transports through the indicated sections at ϕ_c and θ_0. For $\mathcal{R} = 0$, complete leakage occurs (top panel) while for $\mathcal{R} = 1$ there is complete retroflection (bottom panel). Note that the western part of the domain is supposed to be open, as it is in reality. In intermediate cases, there is partial retroflection (middle panel, where also the integration bounds in (4) are indicated).
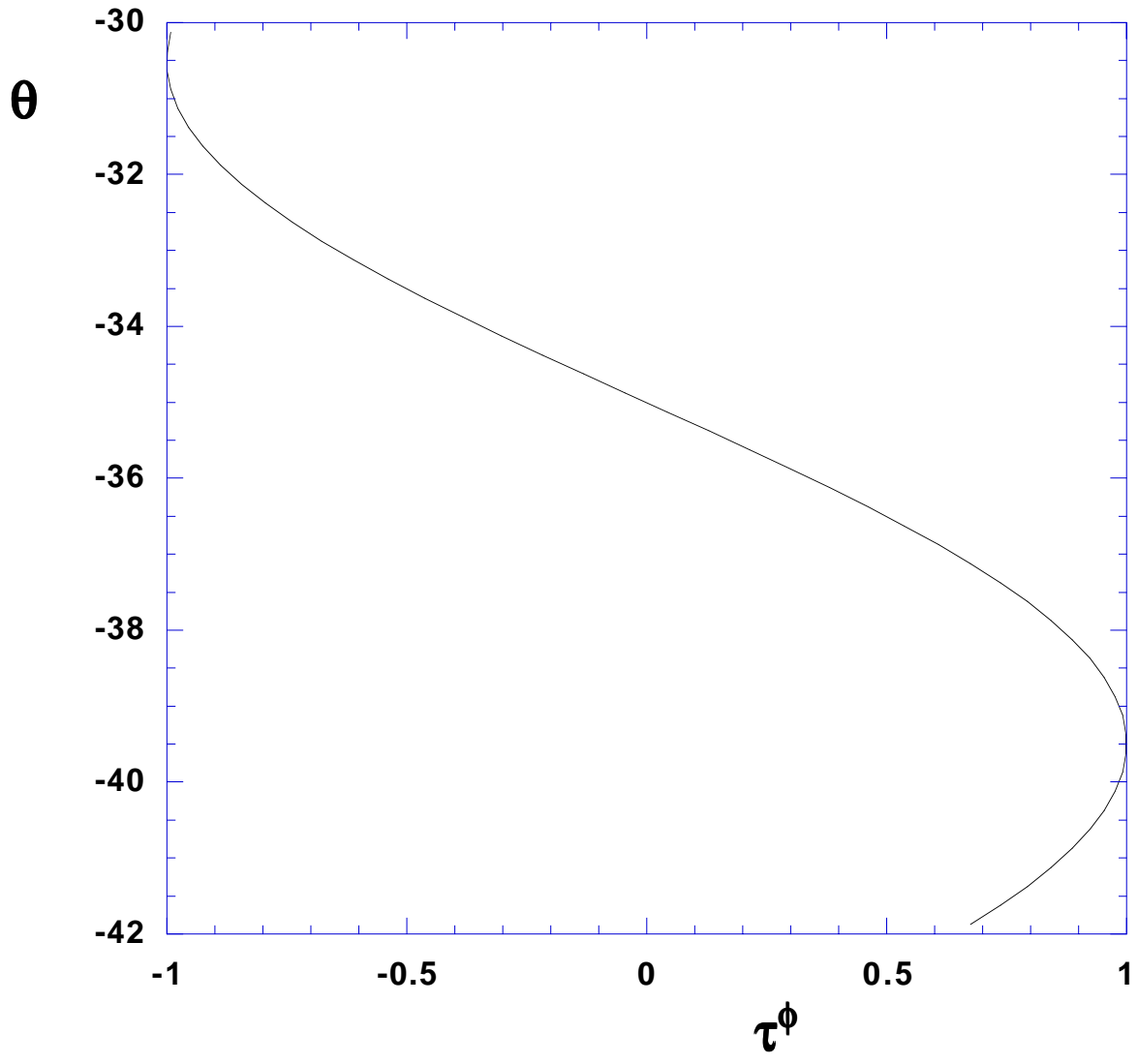
Fig.2

Profile of the wind stress shape function τ^ϕ (9).

Fig. 3

Bifurcation diagram for the standard values of parameters (Table 1) for four different resolutions. On the vertical axis, the retroflection index $\mathcal{R}$ (10) is plotted for each case versus the Ekman number E.

Fig. 4

Solution for the layer thickness anomaly field $\tilde{h} = h - 1$ for $E = 1.1 \times 10^{-7}$ computed at $1/6°$ horizontal resolution. In this and the following contour plots, the fields are scaled with their absolute maximum and contour levels are with respect to this maximum; contour interval is 0.05.

Fig. 5

Bifurcation diagrams for four different layer depths H computed with $1/4°$ resolution. For the depths $H = 1000$ m and $H = 250$ m, the linear stability boundary (a Hopf bifurcation) is indicated by a marker.

Fig. 6

Solutions for the layer thickness anomaly field $\tilde{h}$ at four locations in Fig. 5. (a) $E =$

2.04×10^{-7}, $H = 2000$ m. (b) $E = 2.37 \times 10^{-7}$, $H = 1000$ m. (c) $E = 2.23 \times 10^{-7}$, $H = 500$ m. (d) $E = 2.00 \times 10^{-7}$, $H = 250$ m.

Fig. 7

Terms in the vorticity balance with drawn -F (friction), dashed B (β-effect, dash-dotted -W (wind) and dotted I (inertia)) along the zonal section at $\theta = -35$ for the solutions in Fig. 6. (a) $E = 2.04 \times 10^{-7}$, $H = 2000$ m. (b) $E = 2.37 \times 10^{-7}$, $H = 1000$ m. (c) $E = 2.23 \times 10^{-7}$, $H = 500$ m. (d) $E = 2.00 \times 10^{-7}$, $H = 250$ m.
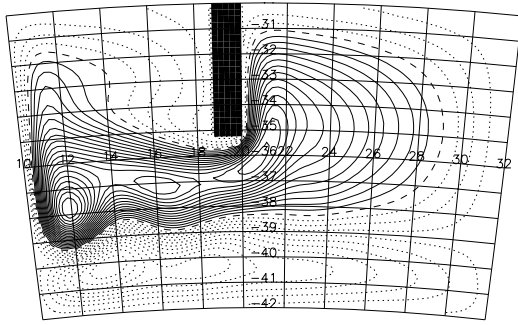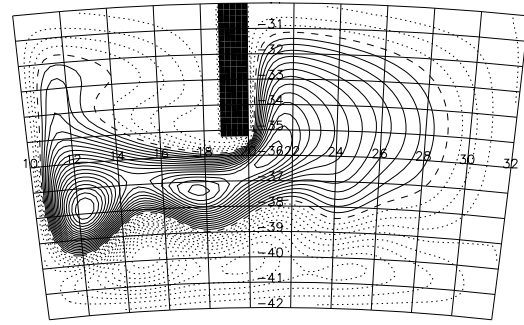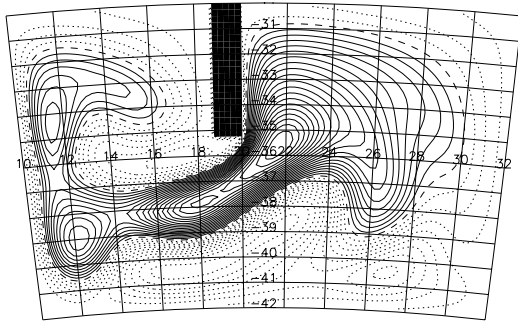
Fig. 8.

Terms in the vorticity balance along a meridional section at $\phi = 20$ (drawn -F (friction), dashed B (β), dash-dotted -W (wind) and dotted I (inertia)) for the solutions in Fig. 6. (a) $E = 2.04 \times 10^{-7}$, $H = 2000$ m. (b) $E = 2.37 \times 10^{-7}$, $H = 1000$ m. (c) $E = 2.23 \times 10^{-7}$, $H = 500$ m. (d) $E = 2.00 \times 10^{-7}$, $H = 250$ m.

Fig. 9.

Contour plot of the zonal (a) wind stress τ^ϕ and (b) meridional wind stress τ^θ over the computational domain. Both fields are scaled with their absolute maximum and contour levels are with respect to this maximum (τ_0 as in Table 2).

Fig. 10.

Bifurcation diagram showing the retroflection index $\mathcal{R}$ versus the Ekman number E for four different layer depths H.

Fig. 11.

Solutions of the layer thickness anomaly for the different cases considered in Fig. 10. (a) $H = 1000$ m at $E = 1.0 \times 10^{-5}$. (b) $H = 1000$ m at $E = 2.9 \times 10^{-7}$. (c) $H = 2000$ m at $E = 3.7 \times 10^{-7}$. (d) $H = 4000$ m at $E = 2.5 \times 10^{-7}$.

Fig. 12.

(a-b) Terms in the vorticity balance along a zonal section at $\theta_0 = -35$ (drawn -F

(friction), dashed B (β), dash-dotted -W (wind) and dotted I (inertia)). (c-d) Same terms, but along the meridional section at $\phi = 20$. (a/c) $H = 2000\ m$ at $E = 1.0 \times 10^{-5}$. (b/d) $H = 1000\ m$ at $E = 2.5 \times 10^{-7}$.

Fig. 13.

Solutions of the layer thickness anomaly for (a) $E = 10^{-5}$ and (b) $E = 4.4 \times 10^{-7}$ using a continental shape as defined in (12) with $\theta_p = -38.5$ and $\gamma = 2.58$.

Fig. 14.

Anomaly of layer thickness for the flow in the domain $[0, 360] \times [-80, 0]$ forced with realistic wind stress. The parameters are standard as in relatistic basin case (Table 2) and $E = 1.7 \times 10^{-5}$.

Table Captions

Table 1.

Standard values of parameters in the barotropic model for the idealized small basin. The value of A_H (and consequently E) is the reference value as used in De Ruijter and Boudra (1985). E will be used here as control parameter and varied over several orders of magnitude.

Table 2.

Standard values of parameters in the set-up of the barotropic model for the case similar to Matano (1996). Again, the Ekman number is a reference value and will be varied in the results here over several orders of magnitude.

Figure 1: *Sketch illustrating the meaning of the retroflection index, which is based on the different volume transports through the indicated sections at ϕ_c and θ_0. For $\mathcal{R} = 0$, complete leakage occurs (top panel) while for $\mathcal{R} = 1$ there is complete retroflection (bottom panel). Note that the western part of the domain is supposed to be open, as it is in reality. In intermediate cases, there is partial retroflection (middle panel, where also the integration bounds in (4) are indicated).*

Figure 2: *Profile of the wind stress shape function τ^ϕ (9).*
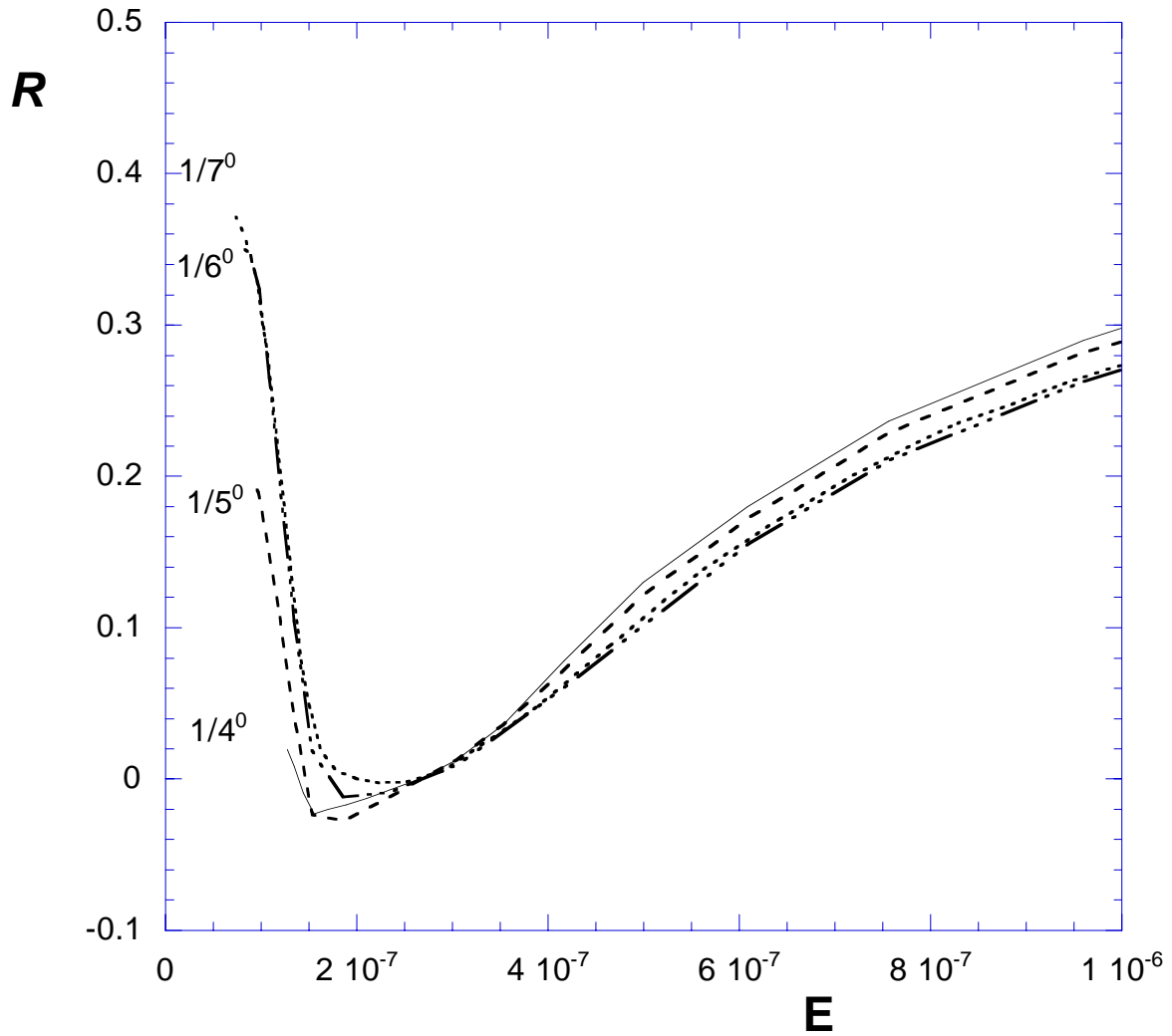
Figure 3: *Bifurcation diagram for the standard values of parameters (Table 1) for four different resolutions. On the vertical axis, the retroflection index $\mathcal{R}$ (10) is plotted for each case versus the Ekman number E.*
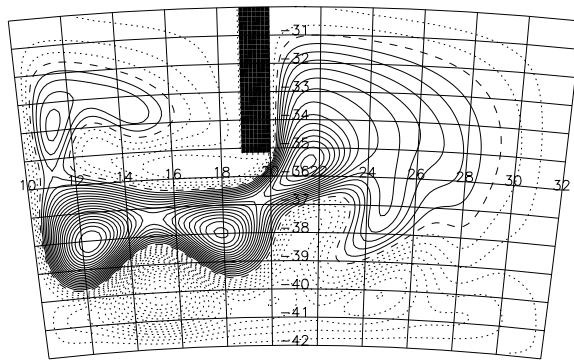
Figure 4: *Solution for the layer thickness anomaly field $\tilde{h} = h - 1$ for $E = 1.1 \times 10^{-7}$ computed at $1/6°$ horizontal resolution. In this and the following contour plots, the fields are scaled with their absolute maximum and contour levels are with respect to this maximum; contour interval is* 0.05.
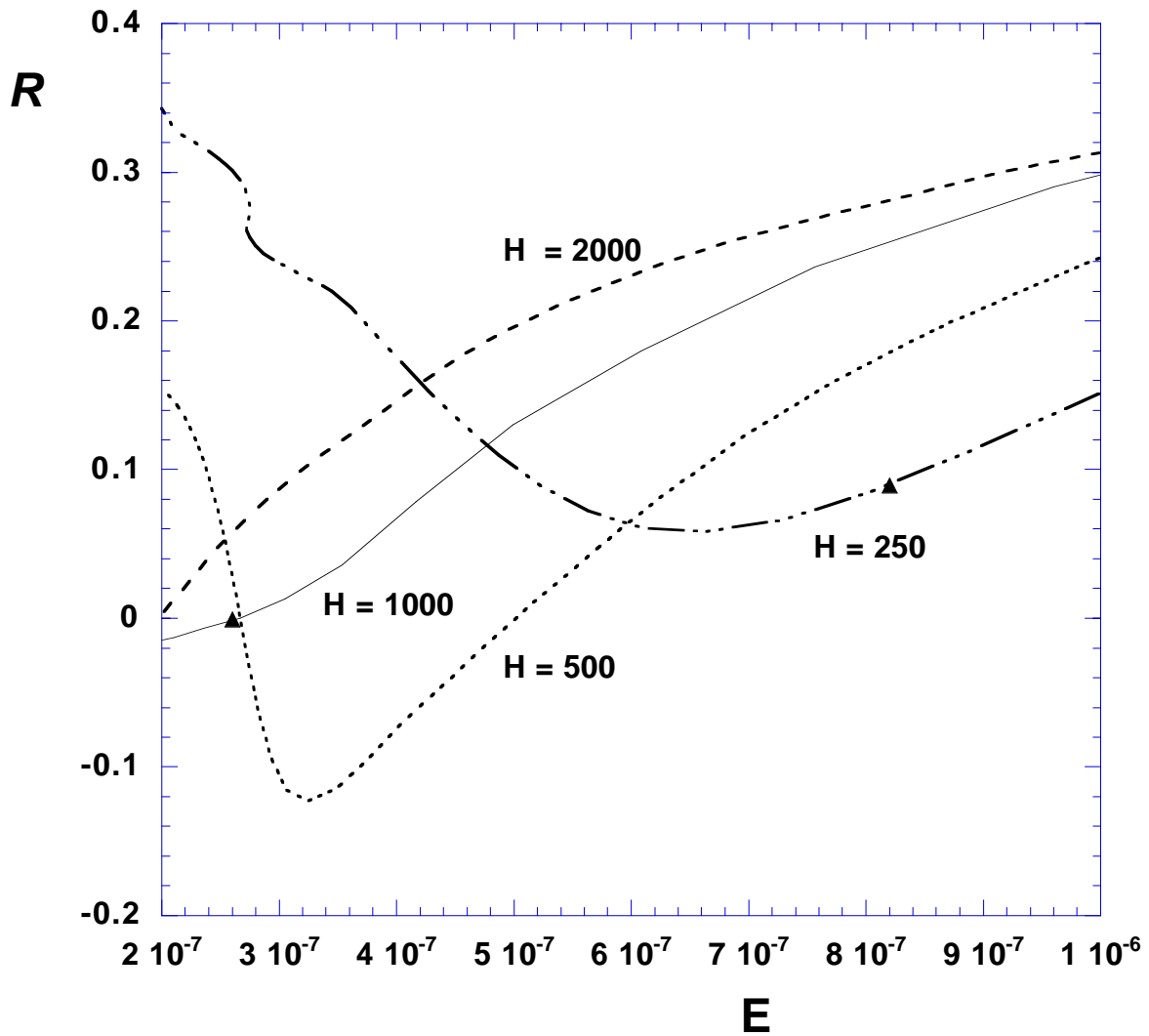
Figure 5: *Bifurcation diagrams for four different layer depths H computed with 1/4° resolution. For the depths H = 1000 m and H = 250 m, the linear stability boundary (a Hopf bifurcation) is indicated by a marker.*

(a)

(b)

(c)

(d)

Figure 6: *Solutions for the layer thickness anomaly field $\tilde{h}$ at four locations in Fig. 5. (a) $E = 2.04 \times 10^{-7}$, $H = 2000$ m. (b) $E = 2.37 \times 10^{-7}$, $H = 1000$ m. (c) $E = 2.23 \times 10^{-7}$, $H = 500$ m. (d) $E = 2.00 \times 10^{-7}$, $H = 250$ m.*
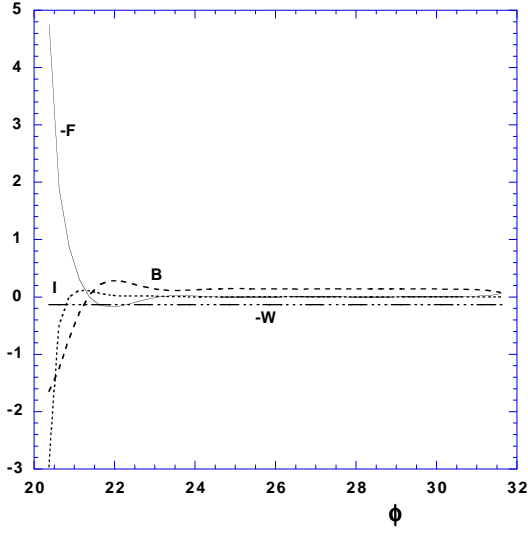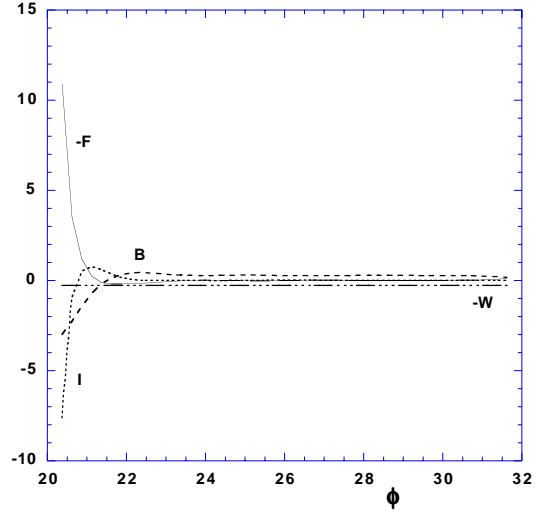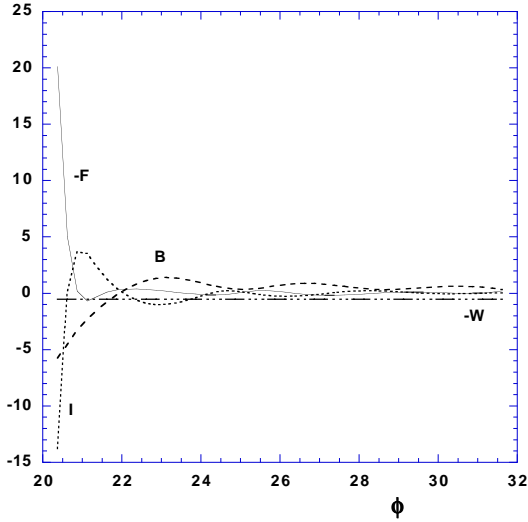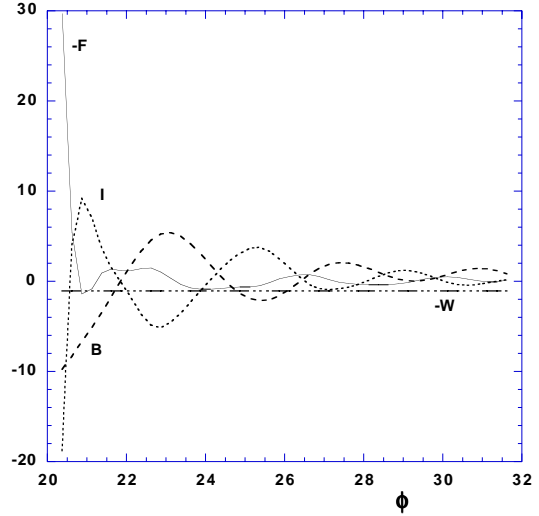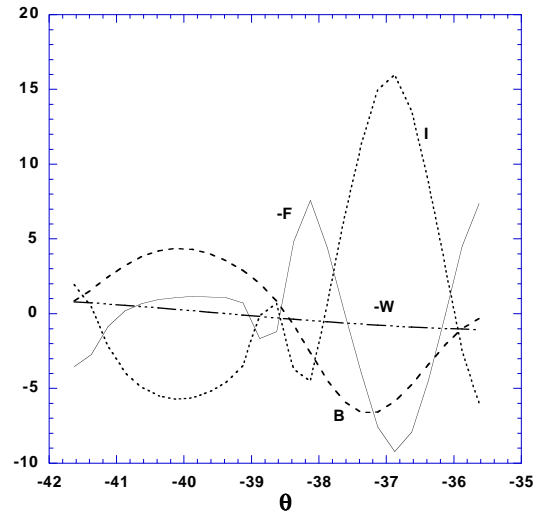
Figure 7: *Terms in the vorticity balance with drawn -F (friction), dashed B (β-effect, dash-dotted -W (wind) and dotted I (inertia)) along the zonal section at θ = −35 for the solutions in Fig. 6. (a) E = 2.04 × 10⁻⁷, H = 2000 m. (b) E = 2.37 × 10⁻⁷, H = 1000 m. (c) E = 2.23 × 10⁻⁷, H = 500 m. (d) E = 2.00 × 10⁻⁷, H = 250 m.*

(a)

(b)

(c)

(d)

Figure 8: *Terms in the vorticity balance along a meridional section at $\phi = 20$ (drawn -F (friction), dashed B (β), dash-dotted -W (wind) and dotted I (inertia)) for the solutions in Fig. 6. (a) $E = 2.04 \times 10^{-7}$, $H = 2000$ m. (b) $E = 2.37 \times 10^{-7}$, $H = 1000$ m. (c) $E = 2.23 \times 10^{-7}$, $H = 500$ m. (d) $E = 2.00 \times 10^{-7}$, $H = 250$ m.*

41
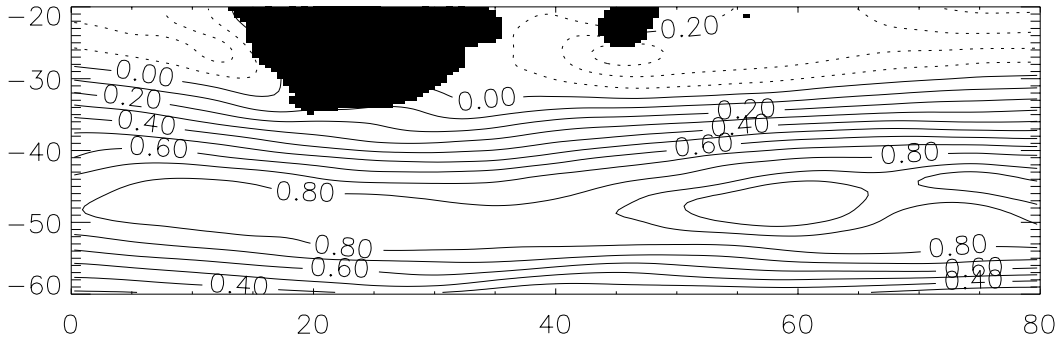
(a)
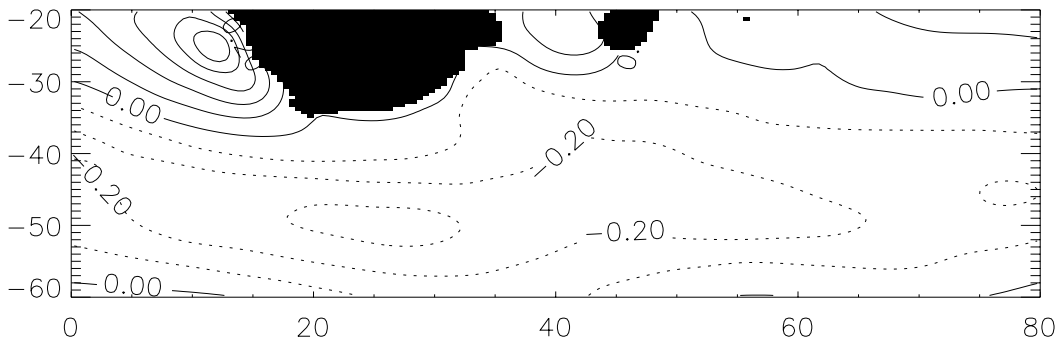
(b)

Figure 9: *Contour plot of the zonal (a) wind stress τ^ϕ and (b) meridional wind stress τ^θ over the computational domain. Both fields are scaled with their absolute maximum and contour levels are with respect to this maximum (τ_0 as in Table 2).*
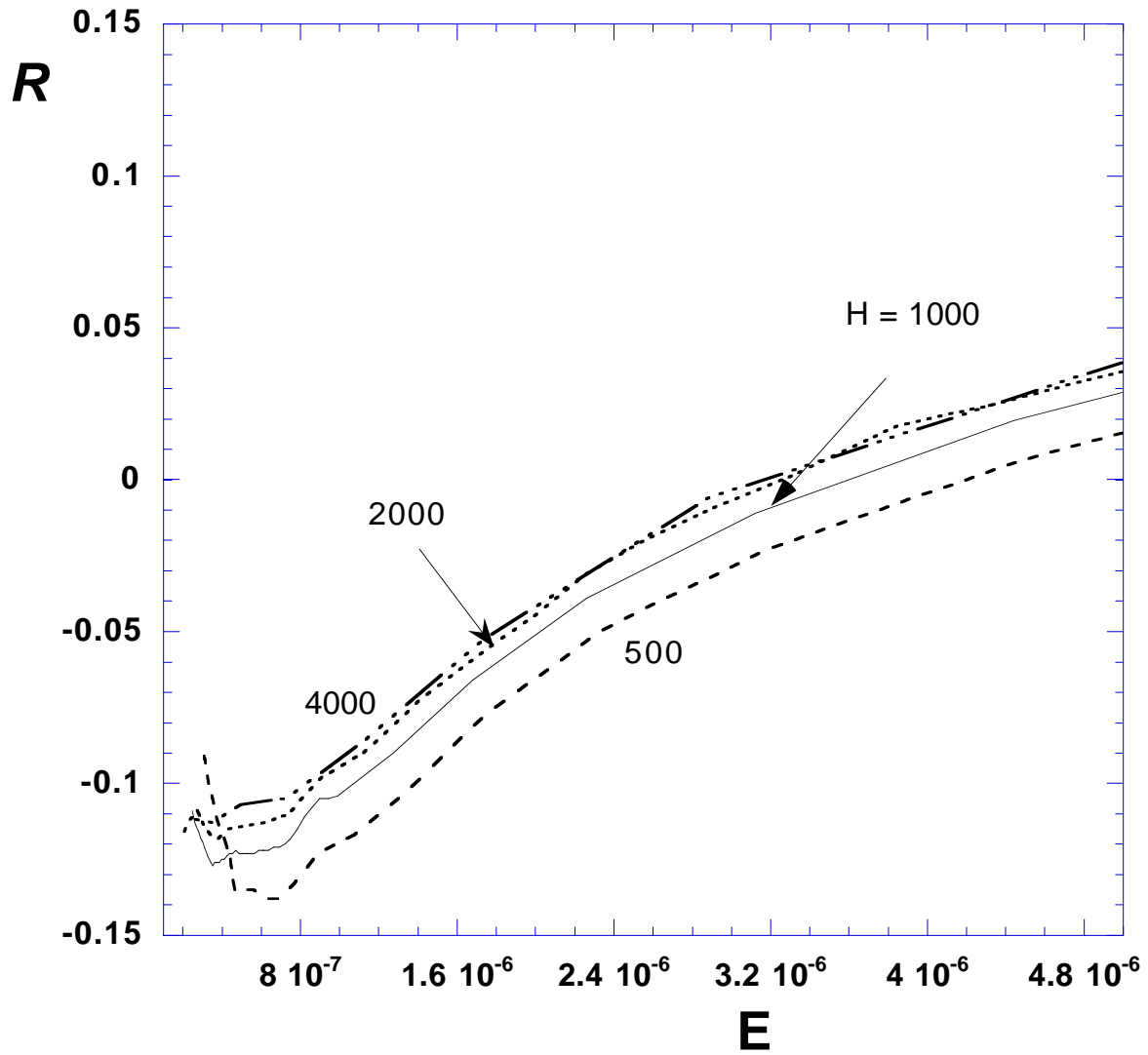
Figure 10: *Bifurcation diagram showing the retroflection index $\mathcal{R}$ versus the Ekman number E for four different layer depths H.*
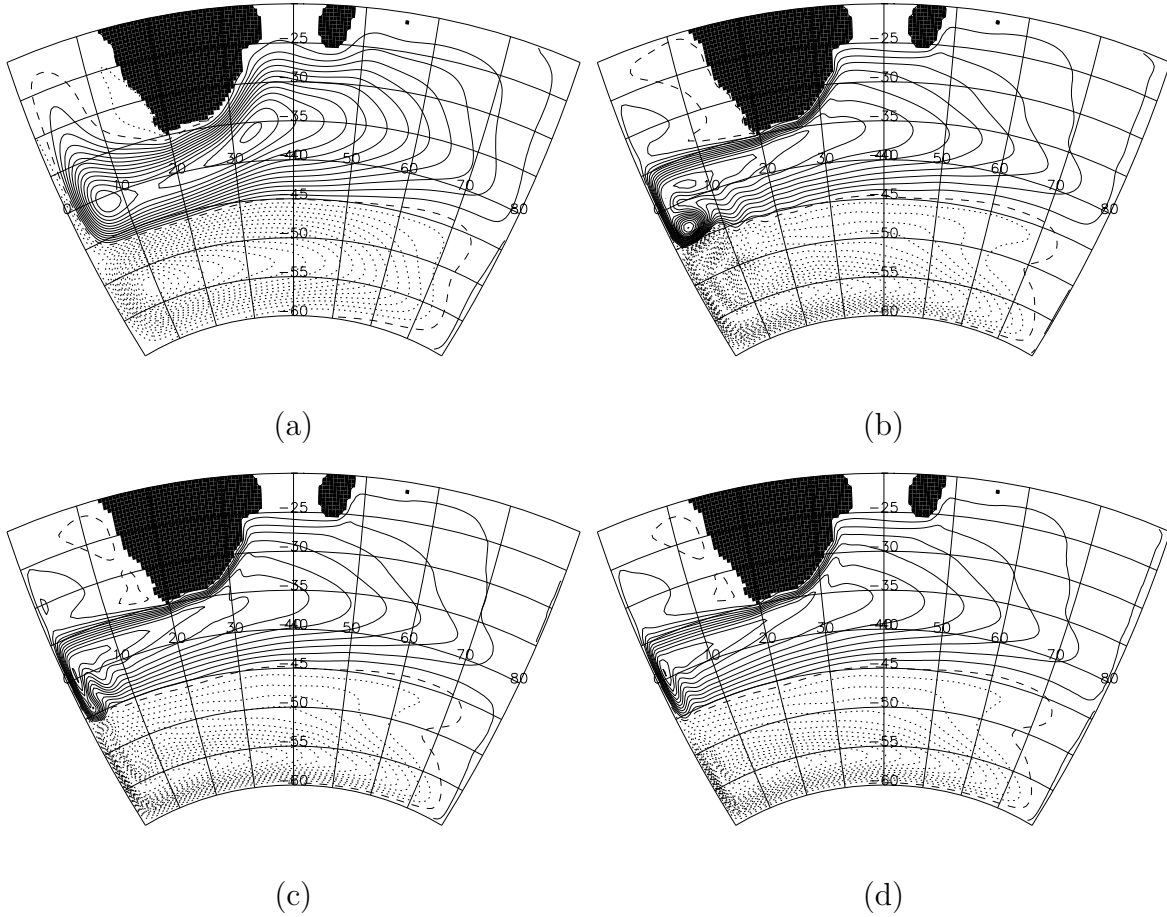
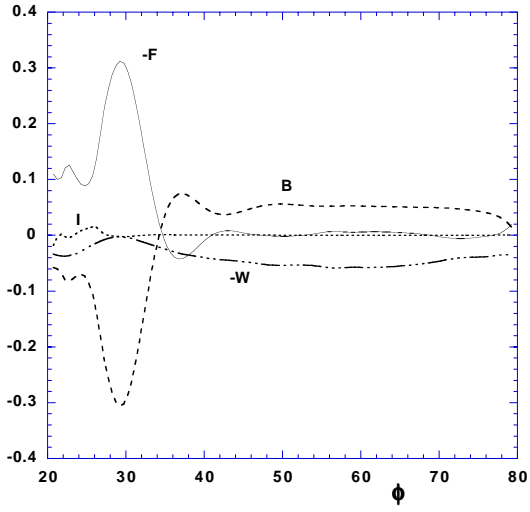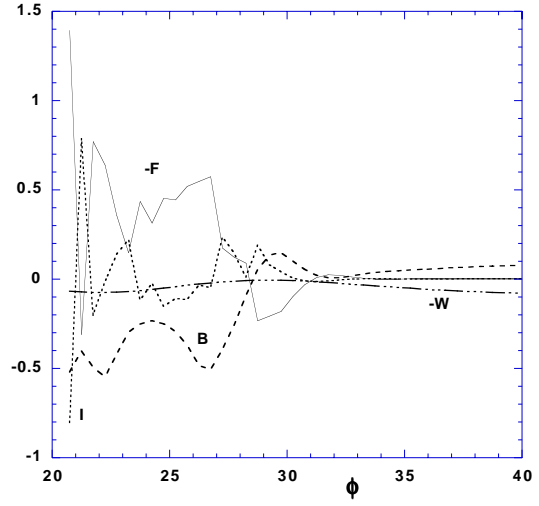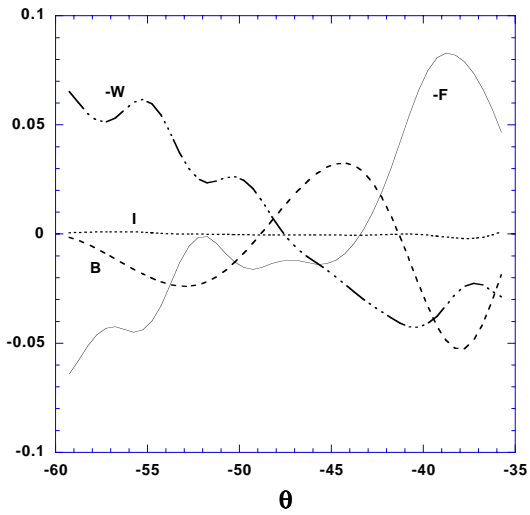(a)   (b)

(c)   (d)

Figure 11: *Solutions of the layer thickness anomaly for the different cases considered in Fig. 10. (a) $H = 1000\ m$ at $E = 1.0 \times 10^{-5}$. (b) $H = 1000\ m$ at $E = 2.9 \times 10^{-7}$. (c) $H = 2000\ m$ at $E = 3.7 \times 10^{-7}$. (d) $H = 4000\ m$ at $E = 2.5 \times 10^{-7}$.*
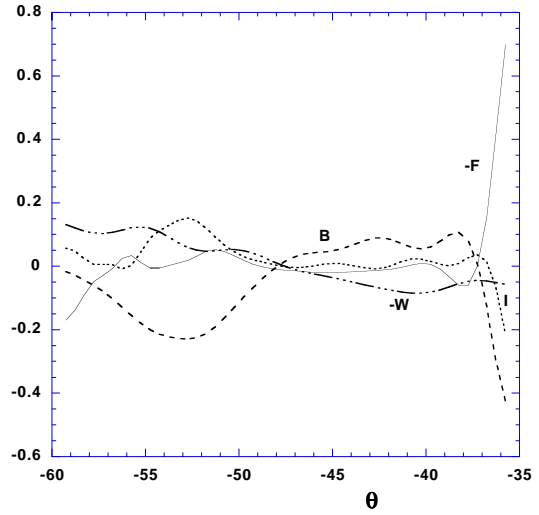
44

(a)

(b)

(c)

(d)

Figure 12: *(a-b) Terms in the vorticity balance along a zonal section at $\theta_0 = -35$ (drawn -F (friction), dashed B (β), dash-dotted -W (wind) and dotted I (inertia)). (c-d) Same terms, but along the meridional section at $\phi = 20$. (a/c) $H = 2000$ m at $E = 1.0 \times 10^{-5}$. (b/d) $H = 1000$ m at $E = 2.5 \times 10^{-7}$.*
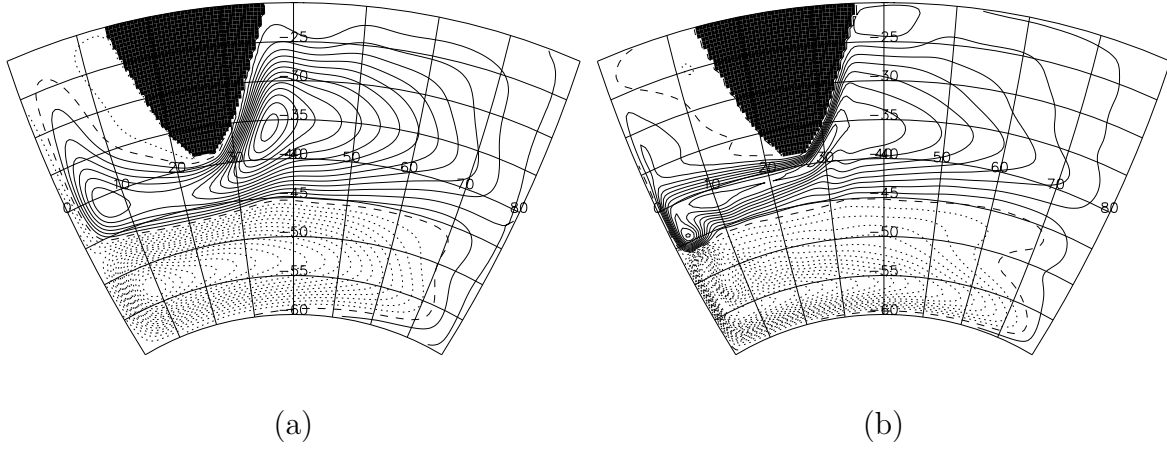
(a)   (b)

Figure 13: *Solutions of the layer thickness anomaly for (a) $E = 10^{-5}$ and (b) $E = 4.4 \times 10^{-7}$ using a continental shape as defined in (12) with $\theta_p = -38.5$ and $\gamma = 2.58$.*
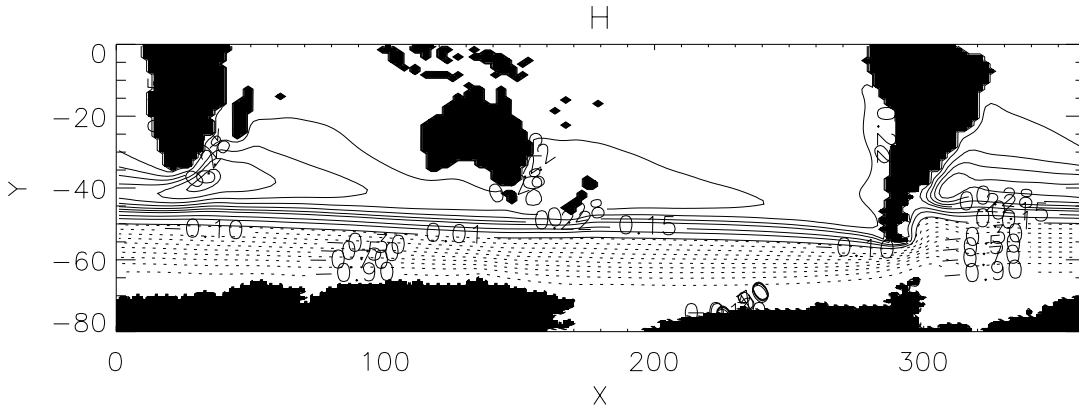

Figure 14: *Anomaly of layer thickness for the flow in the domain $[0, 360] \times [-80, 0]$ forced with realistic wind stress. The parameters are standard as in relatistic basin case (Table 2) and $E = 1.7 \times 10^{-5}$.*

Dimensional parameters			
Parameter	Value	Parameter	Value
r_0	$6.7 \times 10^7\ m$	τ_0	$2.0 \times 10^{-1}\ Pa$
H	$1.0 \times 10^3\ m$	A_H	$3.3 \times 10^2\ m^2 s^{-1}$
g	$9.8\ ms^{-2}$	U	$1.0\ ms^{-1}$
ρ_0	$1.0 \times 10^3\ kgm^{-3}$	Ω	$7.5 \times 10^{-5} s^{-1}$
Dimensionless parameters			
Parameter	Value	Parameter	Value
α	1.4×10^{-3}	E	5.0×10^{-8}
ϵ	1.0×10^{-4}	F	9.8×10^5

Table 1: *Standard values of parameters in the barotropic model for the idealized small basin. The value of A_H (and consequently E) is the reference value as used in De Ruijter and Boudra (1985). E will be used here as control parameter and varied over several orders of magnitude.*

Dimensional parameters			
Parameter	Value	Parameter	Value
r_0	$6.7 \times 10^7 \ m$	τ_0	$3.0 \times 10^{-1} \ Pa$
H	$1.0 \times 10^3 \ m$	A_H	$2.0 \times 10^3 \ m^2 s^{-1}$
g	$9.8 \ ms^{-2}$	U	$1.0 \ ms^{-1}$
ρ_0	$1.0 \times 10^3 \ kgm^{-3}$	Ω	$7.5 \times 10^{-5} s^{-1}$
Dimensionless parameters			
Parameter	Value	Parameter	Value
α	2.1×10^{-2}	E	3.0×10^{-7}
ϵ	1.0×10^{-4}	F	9.8×10^5

Table 2: *Standard values of parameters in the set-up of the barotropic model for the case similar to Matano (1996). Again, the Ekman number is a reference value and will be varied in the results here over several orders of magnitude.*